Universities of Leeds, Sheffield and York
http://eprints.whiterose.ac.uk/

On the formation of cyclones and anticyclones in a rotating fluid

Binod Sreenivasan[1] and P.A. Davidson[2]

[1]*School of Earth and Environment, University of Leeds, Leeds LS2 9JT, United Kingdom.*

[2]*Department of Engineering, University of Cambridge, Cambridge CB2 1PZ, United Kingdom.*

It is commonly observed that the columnar vortices which dominate the large scales in homogeneous, rapidly rotating turbulence are predominantly cyclonic. This has prompted us to ask how this asymmetry arises. To provide a partial answer to this we look at the process of columnar vortex formation in a rotating fluid, and in particular, we examine how a localized region of swirl (an eddy) can convert itself into a columnar structure by inertial wave propagation. We show that, when the Rossby number (Ro) is small, the vortices evolve into columnar eddies through the radiation of linear inertial waves. When the Rossby number is large, on the other hand, no such column is formed. Rather, the eddy bursts radially outward under the action of the centrifugal force. There is no asymmetry between cyclonic and anticyclonic eddies for these two regimes. However, cyclones and anticyclones behave differently in the intermediate

---

[1]Corresponding author; e-mail: binod@earth.leeds.ac.uk

regime of $Ro \sim 1$. Here we find that the transition from columnar vortex formation to radial bursting occurs at lower values of Ro for anticyclones, with the transition for anticyclones occurring at $Ro \sim 0.5$, and that for cyclones at $Ro \sim 2$. Thus, in a homogeneous turbulence experiment conducted at, say, $Ro = 1$, we would expect to see more cyclones than anticyclones. The reason for this asymmetry at $Ro \sim 1$ is explained.

1 Introduction

The motivation for this work stems from the observation that, typically, many more cyclones than anticyclones are observed in homogeneous, rapidly rotating turbulence. While we do not study turbulence here, but rather a more idealized, deterministic problem, it may be worth reviewing briefly the evidence from these turbulent flows.

It is well-known that the large scales in rapidly rotating turbulence tend to be dominated by columnar vortices aligned with the rotation axis (see, for example, Hopfinger et al[1] and Davidson et al[2]). In freely-decaying, homogeneous turbulence these columnar vortices first appear when the Rossby number, $Ro = u/\Omega l$, falls below ~ 1, where Ω is the bulk rotation rate, l a suitably defined integral scale, and u a characteristic velocity of the turbulence measured in the rotating frame of reference. This growth of columnar vortices is clearly evident in the experiments of, say, Davidson et al[2] and Staplehurst et al[3], and the mechanism by which they form is quasi-linear inertial wave propagation.[2,3] That is to say, for $Ro << 1$, eddies (i.e. blobs of vorticity) tend to disperse their energy and momentum by linear inertial wave propagation, and while much of this energy is dispersed randomly, there is a systematic preference for vortex blobs to radiate energy along the rotation axis, elongating the eddies

2

into columnar structures.[2] In homogeneous turbulence this process is observed to occur not only for small Ro, but also for larger Ro, say $Ro \lesssim 1$.[3]

For $Ro \sim 1$, a second, related phenomenon is observed: there are more cyclones than anticyclones, in the sense that the long-lived, intense regions of ω_z are more likely to be positive than negative. (Here ω_z is the vorticity component parallel to $\boldsymbol{\Omega}$, measured in the rotating frame.) This preference for cyclones is clearly evident in the numerical simulations of Bartello et al,[4] van Bokhoven et al[5] and Bourouiba and Bartello,[6] and in the laboratory experiments of Hopfinger et al,[1] Morize et al[7] and Staplehurst et al[3]. In Refs. 3–7, for example, the vorticity skewness, $S = <\omega_z^3> / <\omega_z^2>^{3/2}$, is found to be positive, indicating that large positive values of ω_z are more likely than large negative values.

The reason for the dominance of cyclones is still poorly understood, though several explanations have been offered. For example, Bartello et al[4] note that, in an inertial frame of reference, where the axial vorticity is $\omega_z + 2\Omega$, two-dimensional axisymmetric cyclones of the form $\mathbf{u} = u_\theta(r)\hat{\mathbf{e}}_\theta$ generally satisfy Rayleigh's stability criterion, whereas the corresponding anticyclones are Rayleigh-unstable when Ro exceeds ~ 1. In this picture, then, both cyclones and anticyclones form, but only the former provide stable, long-lived structures at $Ro \sim 1$. An alternative explanation has been put forward by Gence and Frick.[8] They considered the situation in which fully-developed, isotropic turbulence is suddenly subjected to bulk rotation at $t = 0$. (This requires an infinite acceleration). They showed that, at $t = 0$,

$$\frac{\partial}{\partial t} <\omega_z^3> = 0.4\Omega <\omega_i \omega_j S_{ij}>_0 \tag{1}$$

where S_{ij} is the rate-of-strain tensor. Since $<\omega_i \omega_j S_{ij}>$ is positive in mature, isotropic turbulence, the vorticity skewness grows from $S = 0$ at $t = 0$ to $S > 0$ for $t = 0^+$. Note that this second argument is independent of the value of Ro, and depends crucially on the choice

3

of the initial condition.

In this paper we offer a third explanation. We suggest that, at $Ro \sim 1$, it is not that both cyclones and anticyclones form, with the anticyclones subsequently going unstable, but rather that anticyclones are less likely to form in the first place. The argument proceeds by considering the somewhat idealized problem of the fate of isolated blobs of vorticity (eddies) sitting in an otherwise quiescent, rotating fluid. For $Ro << 1$, we know that such blobs will evolve into columnar vortices via inertial wave propagation,[2] and it does not matter if the average rotation of the blob is cyclonic or anticyclonic. For $Ro >> 1$, on the other hand, no such columnar vortex will appear, with the vorticity distribution determined by nonlinear dynamics, i.e. the advection and stretching of vorticity. In the case of a simple, localized region of swirling fluid, for example, the vortex blob bursts radially outward under the action of the centrifugal force, creating a thin annular sheet of vorticity.[9] Again, it does not matter whether the mean rotation of the blob is cyclonic or anticyclonic. The key point, however, is the following. We shall show that, for localized regions of swirl, the transition from columnar vortex formation to radial bursting is surprisingly rapid, and that the nature of this transition depends crucially on whether the vortex is cyclonic or anticyclonic. For the initial conditions considered here, the transition for cyclones occurs in the range $1.4 < Ro < 3$, with columnar vortex formation below $Ro = 1.4$ and centrifugal bursting for $Ro \gtrsim 3$. For anticyclonic blobs, however, the transition occurs at lower values of Ro, around $0.4 < Ro < 1.6$, with columnar vortex formation for $Ro \lesssim 0.4$. Thus, if we consider an initial condition composed of a random sea of vortex blobs with $Ro \sim 1$, one might expect to see more cyclonic columnar vortices emerge than anticyclonic ones. While the model problem considered here is highly idealized, consisting of localized vortex blobs, the results seem consistent with the experimental observations. Moreover, as we shall see,

4

our findings are not peculiar to the particular initial conditions considered here. Indeed, we shall show that any axisymmetric vortex blob in which the angular velocity decreases monotonically with radius behaves in a similar fashion; that is, the transition from columnar vortex formation to radial bursting occurs at a significantly lower Ro for anticyclones.

We conclude this introduction by noting that there is a substantial body of literature which addresses the cyclone-anticyclone asymmetry in geophysical flows, such as shallow-water, quasi-geostrophic turbulence, or rotating-stratified turbulence. (See, for example, Refs. 10–13). This is an altogether more complex problem, where stratification and surface waves can play an important role. Here we ignore such complexities and are motivated by the simpler situation of homogeneous turbulence in the presence of bulk rotation, as discussed in the laboratory experiments and numerical simulations of Refs. 1–8.

2   Theoretical background

In order to place the subsequent discussion in perspective, it is useful to review briefly what we know about the evolution of a localized blob of vorticity in a rotating fluid. We shall consider the cases of $Ro << 1$ and $Ro >> 1$, describing how columnar vortices (Taylor columns) form for low Ro, and how a swirling blob of fluid bursts radially outward to form an annular vortex sheet when $Ro >> 1$. This discussion is brief and based on the detailed analysis of Refs. 2 and 9. We shall also touch briefly on the analogy between swirl and buoyancy, as this will prove useful in the interpretation of our numerical results in Sec. 4 and 5. For simplicity, we shall ignore viscosity throughout.

5

2.1 The formation of columnar vortices at low Rossby number

Consider the initial value problem consisting of a localized blob of vorticity sitting in an otherwise quiescent, rapidly rotating fluid. Let the bulk rotation rate be $\mathbf{\Omega} = \Omega\hat{\mathbf{e}}_z$, the characteristic scale of the blob be δ and a typical velocity scale be u. If $Ro = u/\Omega\delta << 1$ then the inertial force $\mathbf{u}\cdot\nabla\mathbf{u}$ is much weaker than the Coriolis force $2\mathbf{u}\times\mathbf{\Omega}$, and the governing equation of motion can be linearized to give

$$\frac{\partial\mathbf{u}}{\partial t} = 2\mathbf{u}\times\mathbf{\Omega} - \nabla(p/\rho). \tag{2}$$

The subsequent motion then consists of a spectrum of linear inertial waves whose frequency, ϖ, and group velocity, $\mathbf{c}_g$, are dictated by the initial distribution of wave vectors $\mathbf{k}$, according to

$$\varpi = \pm 2\,(\mathbf{\Omega}\cdot\mathbf{k})/|\mathbf{k}|; \tag{3}$$

$$\mathbf{c}_g = \pm 2\,\mathbf{k}\times(\mathbf{\Omega}\times\mathbf{k})/|\mathbf{k}|^3. \tag{4}$$

For an arbitrarily shaped blob of vorticity we might expect the corresponding spectrum of wave vectors to be equally random, and so (4) suggests that energy and vorticity will disperse in all directions with a typical speed $|\mathbf{c}_g| \sim \Omega\delta$. However, Davidson et al[2] have shown that this radiation of energy is subject to a powerful constraint, which systematically favours dispersion along the rotation axis. In particular, it may be shown that the axial components of the linear and angular impulse of the initial vortex blob (measured in the rotating frame) are confined for all time to the cylindrical region which circumscribes the vortex at $t = 0$. Thus linear and angular momentum can disperse along the rotation axis only. It is clear that this constraint systematically biases the dispersion of energy. For example, as energy radiates to fill a volume of size $\sim (c_g t)^3 \sim (\Omega t\delta)^3$, we could expect the velocity outside

the tangent cylinder to fall as $|\mathbf{u}| \sim |\mathbf{u}_0|(\Omega t)^{-3/2}$. However, inside the tangent cylinder the angular momentum is confined to a cylindrical region of size $\sim c_g t \delta^2 \sim \Omega t \delta^3$, and so the characteristic velocity inside the cylinder falls more slowly, as $|\mathbf{u}| \sim |\mathbf{u}_0|(\Omega t)^{-1}$. (See Ref. 2.) These predictions are readily confirmed by, say, the method of stationary phase.

A simple, almost trivial, example illustrates the point. Suppose our initial condition consists of

$$\mathbf{u} = \Lambda r \exp\left[-(r^2 + z^2)/\delta^2\right] \hat{\mathbf{e}}_\theta \tag{5}$$

in cylindrical polar coordinates, where Λ is a measure of the initial vortex strength. Then (2) yields the axisymmetric wave equation

$$\frac{\partial^2}{\partial t^2} \nabla_*^2 \Gamma + (2\Omega)^2 \frac{\partial^2 \Gamma}{\partial z^2}, \tag{6}$$

where $\Gamma = r u_\theta$ and ∇_*^2 is the Laplacian-like operator

$$\nabla_*^2 \Gamma = r \frac{\partial}{\partial r} \frac{1}{r} \frac{\partial \Gamma}{\partial r} + \frac{\partial^2 \Gamma}{\partial z^2}. \tag{7}$$

This may be readily solved using a Hankel-cosine transform, which yields,[2]

$$u_\theta \approx \Lambda \delta \int_0^\infty \kappa^2 e^{-\kappa^2} J_1(2\kappa r/\delta) \left[\exp\left[-\left(\frac{z}{\delta} - \frac{\Omega t}{\kappa}\right)^2\right] + \exp\left[-\left(\frac{z}{\delta} + \frac{\Omega t}{\kappa}\right)^2\right]\right] d\kappa \tag{8}$$

where J_1 is the usual Bessel function, $\kappa = k_r \delta/2$ and k_r is the radial wavenumber. Evidently, the kinetic energy disperses along the z-axis, forming two columnar structures (Taylor columns) whose centres are located at $z = \pm \delta \Omega t$ and whose lengths grow as $l_z \sim \delta \Omega t$. This is illustrated in Figure 1. Note that the fate of the vortex is independent of whether it is cyclonic or anticyclonic. The precise form of (8) for $\Omega t >> 1$ may be found by insisting that the arguments in the exponentials remain of order unity as $\Omega t \to \infty$. At location $z = \delta \Omega t$, for example, we have

$$u_\theta(r, z = \delta \Omega t) \approx \Lambda \delta (\pi^{1/2}/e) J_1(2r/\delta)(\Omega t)^{-1}, \ \ \Omega t \to \infty, \tag{9}$$

7

which gives $u_\theta \sim \Lambda\delta(\Omega t)^{-1}$ within the tangent cylinder, $r < \delta$, and $u_\theta \sim \Lambda\delta(\Omega t)^{-3/2}(r/z)^{-1/2}$ for $r >> \delta$, in line with the discussion above.

The experiments described in Refs. 2 and 3 show that this kind of linear inertial wave propagation lies behind the columnar structures observed in rotating turbulence when $Ro \sim 1$.

2.2   The radial bursting of a Gaussian vortex for $Ro >> 1$

Let us now consider the opposite extreme, in which the Rossby number is large. For simplicity we consider the same initial condition as before, i.e. (5). This problem is discussed in detail in Ref. 9 and we merely summarise the key results. Since we are considering the limit of $Ro \to \infty$, or $\Omega \to 0$, our frame of reference reverts to an inertial frame. Our inviscid Gaussian vortex now evolves according to,

$$\frac{D\Gamma}{Dt} = 0, \tag{10}$$

$$\frac{D}{Dt}\left(\frac{\omega_\theta}{r}\right) = \frac{1}{r^4}\frac{\partial\Gamma^2}{\partial z} \tag{11}$$

where $\Gamma = ru_\theta$ and ω_θ is the azimuthal vorticity. At $t = 0$, the poloidal velocity, $\mathbf{u}_p = (u_r, 0, u_z)$, is zero by virtue of our choice of initial condition, and so $\boldsymbol{\omega}_\theta = \nabla \times \mathbf{u}_p$ is also zero. However, it is clear from (11) that ω_θ is non-zero for $t > 0$ and the source of this vorticity is evident: the right-hand side of (11) has its roots in $\nabla \times (\mathbf{u}_\theta \times \boldsymbol{\omega}_p)$, and so ω_θ is produced whenever differential rotation (axial gradients in Γ) spiral up the poloidal vortex lines, $\boldsymbol{\omega}_p = \nabla \times [(\Gamma/r)\hat{\mathbf{e}}_\theta]$. This produces a skew-symmetric distribution in ω_θ, with $\omega_\theta < 0$ for $z > 0$ and $\omega_\theta > 0$ for $z < 0$.

The subsequent development of the vortex is easy to predict. The poloidal velocity associated

8

with ω_θ sweeps the Γ-lines radially outward in accordance with (10), and as shown in Figure 2. Integrating (11) yields

$$\frac{d}{dt}\int_{z<0}\frac{\omega_\theta}{r}dV = 2\pi\int_0^\infty \frac{\Gamma_0^2}{r^3}dr, \tag{12}$$

where $\Gamma_0(r) = \Gamma(r, z = 0)$ is the angular momentum density on the symmetry plane. Thus, the integral of $|\omega_\theta/r|$ increases monotonically as the Γ-lines get swept radially outward. Eventually the Γ-lines form a thin axisymmetric sheet as shown in Figure 2, and since Γ is the Stokes stream function for $\boldsymbol{\omega}_p$, this is a poloidal vortex sheet. The mushroom-like shape of this vortex sheet is reminiscent of a thermal plume and indeed there are close analogies to buoyancy, as discussed in Sec. 2.3. In Ref. 9, it is shown that, at large times, the vortex sheet propagates radially outward with constant velocity while thinning exponentially fast.

Evidently, the fate of our Gaussian vortex is radically different depending on whether $Ro <<$ 1 or $Ro >> 1$. The only thing the two limits have in common is that it does not matter whether the initial vortex is cyclonic or anticyclonic. The main purpose of this paper is to explore the intermediate regime of $Ro \sim 1$, and in particular the transition from columnar vortex formation to radial bursting. Our primary finding is that the transition occurs over a surprisingly small range of Ro, and that the nature of the transition depends crucially on whether the initial vortex is cyclonic or anticyclonic. Before examining the numerical evidence, however, it is worth reviewing one last topic: the analogy between swirl and buoyancy. This will help in the interpretation of our results.

2.3   The analogy between swirl and buoyancy

Consider an inviscid, axisymmetric flow evolving in an infinite domain which may or may not have background rotation. We shall find it convenient to temporarily adopt an inertial

9

frame of reference, so that any bulk rotation is absorbed into $\mathbf{u}$. In such a case, axisymmetric flows with swirl have a well-known analogy to flows driven by buoyancy. Consider (10) and (11) rewritten as

$$\frac{D\mathbf{u}_p}{Dt} = -\nabla(p/\rho) + \frac{\Gamma^2}{r^3}\hat{\mathbf{e}}_r, \quad \nabla.\mathbf{u}_p = 0, \tag{13}$$

$$\frac{D\Gamma^2}{Dt} = 0. \tag{14}$$

Compare these with the governing equations for a diffusionless, Boussinesq fluid with density perturbation ρ' and mean density ρ:

$$\frac{D\mathbf{u}}{Dt} = -\nabla(p/\rho) + T\mathbf{g}, \quad \nabla.\mathbf{u} = 0, \tag{15}$$

$$\frac{DT}{Dt} = 0, \tag{16}$$

where $T = \rho'/\rho$ and $\mathbf{g}$ is the gravitational acceleration. Equating Γ^2 to T and $r^{-3}\hat{\mathbf{e}}_r$ to $\mathbf{g}$ provides an exact analogy. Thus, we could interpret (13) and (14) as a poloidal flow driven by density perturbations, Γ^2, in a fictitious radial gravity field, $\mathbf{g} = r^{-3}\hat{\mathbf{e}}_r$. In doing so, we have reduced the problem to that of a strictly poloidal flow evolving in the (r, z) plane. In this analogy, 'heavy' fluid corresponds to large Γ^2, while 'light' fluid corresponds to small values of Γ^2, and potential energy is released whenever heavy fluid moves radially outward, displacing lighter fluid. Indeed, it is readily confirmed that the potential energy density corresponding to the materially conserved density perturbation, $T = \Gamma^2$, moving in the fictitious radial gravity field, $\mathbf{g} = r^{-3}\hat{\mathbf{e}}_r$, is simply $\frac{1}{2}u_\theta^2$. Thus the conservation of kinetic energy

$$E = \frac{1}{2}\int u_\theta^2 dV + \frac{1}{2}\int \mathbf{u}_p^2 dV \tag{17}$$

in the original problem is now interpreted as the conservation of potential energy, $\frac{1}{2}\int u_\theta^2 dV$, plus kinetic energy, $\frac{1}{2}\int \mathbf{u}_p^2 dV$. The radial bursting of the Gaussian eddy in Sec. 2.2 is now

10

easy to interpret. We have a region of heavy fluid immersed in lighter fluid, and this wants to move radially outward under the action of the gravitational field $\mathbf{g} = r^{-3}\hat{\mathbf{e}}_r$. In doing so, it releases potential energy, increasing the kinetic energy of the poloidal flow.

This analogy also provides a simple interpretation of the linear axisymmetric inertial waves discussed in Sec. 2.1. In an inertial frame the background rotation, $\Gamma = \Omega r^2$, represents a radially stratified density field and the inertial waves may be interpreted as small-amplitude internal gravity waves propagating in the fictitious radial gravity field. Indeed, Rayleigh derived his famous stability criterion for the steady flow $\mathbf{u} = u_\theta(r)\hat{\mathbf{e}}_\theta$ using precisely this line of reasoning. That is to say, he converted the problem of the stability of the non-static equilibrium, $\mathbf{u} = u_\theta(r)\hat{\mathbf{e}}_\theta$, to the problem of the static equilibrium, $\mathbf{u}_p = 0$; $\Gamma^2 = \Gamma^2(r)$, observing that stable configurations are the ones in which light fluid lies closer to the axis than heavy fluid, i.e. $\partial\Gamma^2/\partial r > 0$, while unstable configurations correspond to heavy fluid immersed in an annulus of lighter fluid, $\partial\Gamma^2/\partial r < 0$. In short, Rayleigh's stability criterion represents the trivial statement that the flow is stable if and only if the radial stratification $\Gamma^2(r)$ is stable under the action of the radial gravity field $\mathbf{g} = r^{-3}\hat{\mathbf{e}}_r$.

It might be noted that the trick employed by Rayleigh, of converting to the analogous buoyancy problem, is not as *ad hoc* as it might seem. It is a particular example of a more general procedure in Hamiltonian mechanics, called Routh's procedure, in which the symmetries of a problem (the 'ignorable coordinates' in language of Hamiltonian mechanics) can be used to eliminate the corresponding degrees of freedom.[14,15]

We shall find the analogy to buoyancy particularly useful in Sec. 4 and 5 when we investigate the evolution of a localized blob of vorticity immersed in a rotating fluid. The advantage of this analogy is that it provides a particularly simple interpretation of the numerical findings, though its disadvantage is that it requires us to revert to an inertial frame of reference, which

is not the natural frame when discussing localized disturbances in a rotating fluid. One of our main findings is that initial conditions which, in an inertial frame, contain regions in which $\partial \Gamma^2/\partial r < 0$ (heavy fluid immersed in light fluid) tend to burst radially outward, rather than form columnar vortices. On the other hand, initial conditions in which $\partial \Gamma^2/\partial r > 0$ invariably form columnar vortices. Note that this is not a trivial consequence of Rayleigh's stability theorem, as the initial conditions are not steady and so it is meaningless to talk about whether or not they are linearly stable. (One can only talk about the stability of steady solutions of the governing equations.) This is why we suggest that, in rotating turbulence, the prevalence of cyclones is not because columnar anticyclones form and then go Rayleigh-unstable, but rather that they are less likely to form in the first place. Nevertheless, there is clearly a strong physical link between our observation of the importance of $\partial \Gamma^2/\partial r$ and Rayleigh's stability criterion.

3   An outline of the computations

3.1   Problem specification and numerical strategy

We compute the initial value problem of a localized vortex evolving in a rotating fluid. We use a non-inertial frame of reference rotating with the fluid, though on occasions it will prove convenient to revert to an inertial frame. To distinguish between the two, we use $\hat{()}$ to denote a quantity measured in the inertial frame. Thus, for example,

$$\hat{\Gamma} = \Omega r^2 + \Gamma. \tag{18}$$

The initial condition, in the rotating frame of reference, is axisymmetric and takes the form

$$\mathbf{u} = \Lambda r \frac{(r^2 + z^2)^{1/2}}{\delta} \exp\left[-(r^2 + z^2)/\delta^2\right]\hat{\mathbf{e}}_\theta. \tag{19}$$

The flow is nominally inviscid, though we incorporate a small but finite viscosity in order to ensure numerical stability. The initial Reynolds number, based on δ and the maximum velocity at $t = 0$, is $Re = 5000$. For large values of Ro steep radial gradients in Γ develop, as discussed in Sec. 2.2. In order to ensure that there is adequate resolution in the simulations we track the maximum value of $\hat{\Gamma}$, which should be conserved in an inviscid flow. If $\hat{\Gamma}$ was found to drop by more than 2.5% of its initial value, the simulation was stopped. Note, however, that tests with increased resolution showed that much of the fall in $\hat{\Gamma}$ was due viscous diffusion, rather than due to a loss of resolution.

The numerical scheme is described in Ref. 9 and uses spherical polar coordinates[16] expanded in terms of spherical harmonics, is spectral in the azimuthal angle and colatitude, and employs finite differences in the radial coordinate. The initial computations for anticyclonic vortices at $Ro = 0.1$, 1.0 and 2.0 were fully three-dimensional and these showed that the flow remains axisymmetric. Moreover, when a 2% non-axisymmetric perturbation (of azimuthal wavenumber $m = 4$) was introduced into the $Ro = 1$ initial condition, the flow remained close to axisymmetric, with no leakage of energy into the non-axisymmetric modes. In short, the trajectory of the flow is stable to small but finite non-axisymmetric disturbances. Consequently, subsequent computations took advantage of assumed axial symmetry, with the number of radial nodes set equal to 5000. The flow domain is spherical with a radius of R set equal to 10δ. This allowed the vortex to undergo significant evolution without the effects of the confinement becoming important. No-slip boundary conditions were used in all calculations. Both cyclonic ($\Lambda > 0$) and anticyclonic ($\Lambda < 0$) initial conditions were investigated, with Ro ranging from 0.01 up to 5. It is convenient to define Ro as $|u_{max}|/2\Omega\delta$,

13

where u_{max} is the maximum velocity at $t = 0$. For initial condition (19) this gives,

$$Ro = |\Lambda|/2e\Omega. \tag{20}$$

3.2 The topology of the initial condition

Since $D\hat{\Gamma}/Dt = 0$ in an inviscid fluid, the topology of the $\hat{\Gamma}$-lines must be conserved. Thus, whatever topology is built in at $t = 0$ is preserved throughout the simulation and this imposes constraints on the way in which the flow can evolve. The nature and consequences of these topological constraints change with Ro, and so, before discussing the simulations, it is useful to look at how the shape of the initial $\hat{\Gamma}$-lines varies with Ro. From (19) and (20) we have

$$\hat{\Gamma} = \Omega r^2 \pm (2eRo)\Omega r^2 \frac{(r^2 + z^2)^{1/2}}{\delta} \exp\left[-(r^2 + z^2)/\delta^2\right]. \tag{21}$$

Consider first cyclonic initial conditions, corresponding to the plus sign in (21). Here it is readily confirmed that there are two regimes. For $Ro < 1.388$, the $\hat{\Gamma}$-lines are topologically equivalent to the unperturbed case, with all the $\hat{\Gamma}$-lines unclosed. For $Ro > 1.388$, however, an isolated region of closed $\hat{\Gamma}$-lines appears, as shown in Figure 3. There is a local maximum in $\hat{\Gamma}$ at the centre of the island, and a saddle point to the right. The width of the island can be shown to grow approximately as $\sim 0.61\delta \ln(Ro/1.388)$. The main significance of the appearance of this region of closed $\hat{\Gamma}$-lines is that, to the right of the local maximum in $\hat{\Gamma}$, there is a region in which $\partial\hat{\Gamma}^2/\partial r < 0$. We might expect, therefore, that $Ro = 1.388$ heralds the beginning of the transition from columnar vortex formation to the radial bursting of the vortex.

The case of anticyclonic initial conditions is slightly more complicated. Here there are three regimes. For $Ro < 0.377$ the $\hat{\Gamma}$-lines are all unclosed, topologically equivalent to the

14

unperturbed flow. However, for $0.377 < Ro < 0.429$ an island of closed $\hat{\Gamma}$-lines appears, similar to that of the cyclonic case. There is a local maximum in $\hat{\Gamma}$ at the centre of the island, and a saddle point to the right. The width of the island grows faster than for cyclones, approximately as $\sim 1.9\delta \ln(Ro/0.377)$. As Ro increases, the value of the $\hat{\Gamma}$-line which encircles the island decreases until, at $Ro = 0.429$, the bounding $\hat{\Gamma}$-line reaches a value of zero and connects to the axis. We then enter a new regime in which we have two regions of closed $\hat{\Gamma}$-lines, both of which are topologically connected to the axis of symmetry. The inner one encloses a region of positive $\hat{\Gamma}$ and has a local maximum in $\hat{\Gamma}$ near its centre. Surrounding this there is region of closed $\hat{\Gamma}$-lines in which $\hat{\Gamma}$ is negative. This encloses a local minimum in $\hat{\Gamma}$. In both regions, we find $\partial\hat{\Gamma}^2/\partial r < 0$ (heavy fluid immersed in lighter fluid) to the right of the local extremum in $\hat{\Gamma}$. The various regimes are shown in Figure 4. Note that, as Ro increases, the inner region of closed $\hat{\Gamma}$-lines shrinks at the expense of the outer region of negative $\hat{\Gamma}$, and that by $Ro = 0.8$, the former has all but disappeared. So, for $Ro > 0.8$, the dominant region of potentially unstable fluid ($\partial\hat{\Gamma}^2/\partial r < 0$) lies between the minimum in $\hat{\Gamma}$ and the bounding curve $\hat{\Gamma} = 0$.

Since the topology of the $\hat{\Gamma}$-lines is preserved for all time, we might expect columnar anticyclones to emerge for $Ro < 0.377$, with a gradual transition to radial bursting as Ro increases. Integrating

$$\frac{D}{Dt}\Big(\frac{\hat{\omega}_\theta}{r}\Big) = \frac{\partial}{\partial z}\Big(\frac{\hat{\Gamma}^2}{r^4}\Big) = \nabla \cdot \big[(\hat{\Gamma}^2/r^4)\hat{\mathbf{e}}_z\big] \tag{22}$$

we find that, for anticyclonic initial conditions,

$$\frac{d}{dt}\int_{z<0} \frac{\hat{\omega}_\theta}{r}dV = 2\pi \int_0^\infty \big[(\hat{\Gamma}_0^2 - (\Omega r^2)^2)/r^3\big]dr = \frac{e^2}{2}\Omega^2 Ro\,\delta^2\big[Ro - \frac{2\sqrt{\pi}}{e}\big], \tag{23}$$

which is reminiscent of (12) for the non-rotating case. Thus the mean azimuthal vorticity changes sign at $Ro = 1.30$, and we might anticipate that this heralds a change in behaviour.

In particular, we would expect the radial velocity on the symmetry plane to change from inward to outward, marking the beginning of a tendency for the vortex to burst radially outward. We shall see that this is indeed the case.

4   The behaviour of anticyclonic vortices

We now present the results of the numerical simulations, starting with anticyclonic initial conditions. Noting that topological changes in the initial distribution of $\hat{\Gamma}$ occur at $Ro = 0.377$ and $Ro = 0.429$, and that there is a change in the sign of $\int_{z<0}(\omega_\theta/r)dV$ at $Ro = 1.30$, we might expect to pass through several regimes as we move from small to large Ro. In fact, we shall find it convenient to classify the results, at least approximately, in terms of five ranges of Ro:

1. $Ro < 0.38$; here quasi-linear inertial wave propagation leads to a pair of columnar anticyclones, reminiscent of the behaviour at $Ro \to 0$;

2. $0.38 < Ro < 0.43$; in this case energy spreads predominantly along the rotation axis by inertial wave propagation, but the resulting columnar vortex is fundamentally different in structure to that at lower Ro and this is a result of the topological change which occurs at $Ro = 0.377$;

3. $0.43 < Ro < 0.8$; the vortex still elongates somewhat, but there is little wave-like motion, merely a gradual non-oscillatory slide towards an elongated state;

4. $0.8 < Ro < 1.6$; there is little evidence of wave motion, but a direct competition develops between the confined island of 'heavy' fluid, which pushes radially outward, and the surrounding 'light' fluid which tends to gravitate towards the axis;

16

5. $Ro > 1.6$; the behaviour is dominated by the island of heavy fluid located near the axis which bursts radially outward, reminiscent of the behaviour for $Ro \to \infty$, as discussed in Sec. 2.2.

It is remarkable that the transition from columnar vortex formation and radial bursting occurs for such a narrow range of Ro, from 0.38 to 1.6.

Let us start with the range $Ro < 0.38$. The evolution of the poloidal kinetic energy, E_p, normalized by the initial kinetic energy in the rotating frame, E_0, is shown in Figure 5 for $Ro = 0.01 - 0.7$, along with contour plots of the azimuthal kinetic energy, $\frac{1}{2}u_\theta^2$, for the case $Ro = 0.08$. It is clear that, as in the low-Ro limit, the initial vortex blob splits to form a pair of columnar vortices. In addition, there is some weak, off-axis radiation of energy, which is also part of the low-Ro solution. A similar behaviour is seen for all $Ro < 0.37$. Moreover, for $Ro < 0.35$, the poloidal and azimuthal kinetic energies evolve to a state close to equipartition, $E_p/E_0 \sim 0.5$, which is indicative of wave motion. (We shall discuss the behaviour of E_p/E_0 for $Ro = 0.4, 0.5$ and 0.7 shortly.)

Let us now turn to the range $0.38 < Ro < 0.43$. The contour plots of absolute angular momentum, $\hat{\Gamma}$ are shown in Figure 6 for $Ro = 0.4$ at times $\Omega t = 0.375, 2.5$ and 3.25. It is clear that, as for the regime $Ro < 0.38$, the vortex elongates along the rotation axis. However, the structure of the columnar vortex is fundamentally different. In particular, the topology of the $\hat{\Gamma}$-lines is conserved, so that the existence of an isolated island of closed $\hat{\Gamma}$-lines near the origin restricts the degree to which the angular momentum can disperse. One consequence of this is a residual region of Γ in the vicinity of $z = 0$, which is clearly visible in Figure 6, yet absent in Figure 5. This restricted dispersion of angular momentum is reflected in the energy curves E_p/E_0 shown in Figure 5(a). Here the curve for $Ro = 0.4$

17

drops below equipartition, indicating that the angular momentum trapped near the origin cannot contribute to wave motion.

Consider now the regime $0.43 < Ro < 0.8$. This is characterised by the emergence of two regions of closed $\hat{\Gamma}$-lines, an inner area of positive $\hat{\Gamma}$ and an outer region of negative $\hat{\Gamma}$. The inner region contains a local maximum in $\hat{\Gamma}$ and the outer area a local minimum in $\hat{\Gamma}$. Thus both regions exhibit maxima in $\hat{\Gamma}^2$. As Ro increases the inner region shrinks at the expense of the outer one, and by $Ro = 0.8$ the former has all but disappeared (see Figure 4). The flow corresponding to $Ro = 0.7$ is shown in Figure 7 where Figure 7(a) illustrates the contours of $\hat{\Gamma}$, Figure 7(b) the contours of $\frac{1}{2}u_\theta^2$ and Figure 7(c) the variation of $\partial\hat{\Gamma}/\partial r$ on the symmetry plane. Note that the main region of 'heavy' fluid (large $\hat{\Gamma}^2$) surrounds the local minimum in $\hat{\Gamma}$. It is evident that the dominant motion is a gradual slide towards an elongated state as 'light' fluid pushes up towards the axis, with the local minimum in $\hat{\Gamma}$ moving inward and the saddle points on the z-axis moving away from $z = 0$. Clearly the region of heavy fluid is not yet strong enough to burst radially outward. There is some evidence of dispersion of energy by inertial waves in Figure 7(b), but it is weaker than that shown in Figures 5 and 6. The variations of E_p/E_0 versus Ωt for $Ro = 0.5$ and 0.7 are shown in Figure 5 and it is evident that progressively less energy is transferred to E_p as Ro increases, reflecting the diminished role of inertial waves in redistributing energy.

Turning now to the regime $0.8 < Ro < 1.6$, the behaviour becomes more complicated. There is now a direct competition between the heavy fluid, which lies between the local minimum in $\hat{\Gamma}$ and the bounding curve $\hat{\Gamma} = 0$, and the lighter fluid surrounding it. The heavy fluid wants to burst radially outward while the light fluid tends to push up towards the axis. These two effects are finely balanced, as indicated by the change in the sign of $\int_{z<0}(\omega_\theta/r)dV$ at $Ro = 1.3$. There is little evidence of wave propagation in this regime. Contours of $\hat{\Gamma}$

18

show that the local minimum in $\hat{\Gamma}$ (i.e. heavy fluid) now moves radially outward, and that a radial front starts to form, which is the first sign of bursting-like behaviour. The saddle points on the axis, on the other hand, continue to move away from $z = 0$ as light fluid sweeps up towards the axis. This is illustrated in Figure 8(a) which shows the contours of $\hat{\Gamma}$ for $Ro = 1.4$.

The formation of the front is evident from the plots of $(\partial\hat{\Gamma}/\partial r)_{z=0}$ shown in Figure 8(b) for $Ro = 1, 1.4$ and 1.8. It is convenient to define the centre of the front r_f as the local minimum in $\hat{\Gamma}$, i.e. $(\partial\hat{\Gamma}/\partial r)_{z=0} = 0$, and the characteristic thickness of the front, δ_f, as the distance between the minimum and maximum values of $(\partial\hat{\Gamma}/\partial r)_{z=0}$. Figure 9(a) shows r_f, normalized by its initial value, r_{f0}, as a function of Ωt for the range $0.7 < Ro < 2.0$, while Figure 9(b) shows the front thickness, δ_f, as a function of t/τ, where τ is the initial turn-over time of the eddy, $\delta/u_{max,0}$. Evidently, the location of $\hat{\Gamma}_{min}$ moves inward for $Ro = 0.7$, but outward for $Ro \geq 1$, as suggested above. Moreover, the continual thinning of the front for $Ro \geq 1$ is clearly evident in Figure 9(b). Note, however, that for $Ro < 1.6$ the front thins by $(\partial\hat{\Gamma}/\partial r)_{min}$ moving outward and $(\partial\hat{\Gamma}/\partial r)_{max}$ moving inward, whereas for $Ro > 1.6$, the front thins with both $(\partial\hat{\Gamma}/\partial r)_{min}$ and $(\partial\hat{\Gamma}/\partial r)_{max}$ moving outward, which is characteristic of a bursting vortex in the absence of rotation.[10]

Finally, we consider the regime $Ro > 1.6$. This is characterised by an island of heavy fluid bursting radially outward, reminiscent of the case of $Ro \to \infty$ discussed in Sec. 2.2. In this regime the location of $\hat{\Gamma}_{min}$ moves outward while the saddle points on the axis converge towards $z = 0$. The case of $Ro = 2.0$ is illustrated in Figure 10, where the contours of $\hat{\Gamma}$ are shown in Figure 10(a) and $(\partial\hat{\Gamma}/\partial r)_{z=0}$ is shown in Figure 10(b). Note from Figure 9(b) that the front thins exponentially fast for $Ro > 1.4$, which is the hallmark of the radial bursting of a vortex in the absence of background rotation.[10]

19

In summary, then, for $Ro < 0.4$, an anticyclonic eddy forms a pair of columnar vortices via inertial wave propagation, essentially in the same manner as the linear, low-Ro regime. Conversely, for $Ro > 1.6$, the same vortex bursts radially outward under the action of the centrifugal force, with the background rotation playing almost no role. The intermediate behaviour is quite intricate, but perhaps this is of less interest. The more important point is that there is rapid transition from one regime to the other, at around $Ro \sim 1$.

5   The behaviour of cyclonic vortices

Let us now consider the case of cyclonic vortices. We expect the transition from columnar vortex formation to radial bursting to be more straightforward here, as there is only one topological change in the initial $\hat{\Gamma}$-field, which occurs at $Ro = 1.39$. For $Ro < 1.39$, the $\hat{\Gamma}$-lines are unclosed and topologically equivalent to the unperturbed case, so we might expect columnar vortex formation via quasi-linear inertial wave propagation. For $Ro > 1.39$, an island of closed $\hat{\Gamma}$-lines forms, enclosing a local maximum in $\hat{\Gamma}$, which tends to drive the fluid radially outward. We shall see that quasi-linear columnar vortex formation does indeed occur for $Ro < 1.39$, while radial bursting is the dominant behaviour for $Ro > 3$. For intermediate values of Ro there is evidence of both types of behaviour.

Figure 11 shows the the azimuthal energy density, $\frac{1}{2}u_\theta^2$, for the cases $Ro = 1, 2, 3$ and 4 at $\Omega t = 2.5, 1.0, 0.8$ and 0.5 respectively. It is clear that the dominant behaviour for $Ro = 1$ is axial wave propagation, while radial bursting dominates for $Ro = 3, 4$. The intermediate case of $Ro = 2$ exhibits mixed behaviour, with some dispersion of energy by waves, as well as elements of radial bursting. Figure 12 shows the evolution of $(\partial\hat{\Gamma}/\partial r)_{z=0}$ for the same four values of Ro. The formation of the radial front is evident for $Ro = 3$ and 4, there is no

front for $Ro = 1$, and the behaviour at $Ro = 2$ is more complex, with some evidence of a radial front forming. Finally, Figure 13 shows δ_f versus t/τ, where τ is the initial turn-over time. It is clear that the front thins exponentially fast for $Ro > 3$, which is characteristic of the radial bursting of a vortex in the absence of background rotation. For $Ro = 2$, the front initially thins exponentially fast, but there is a change in behaviour at around $t/\tau = 3.4$.

6 Discussion

The precise details of the transition from columnar vortex formation to centrifugal bursting is, perhaps, not so important, as it depends partly on the particular initial conditions under consideration. The more important observation is that 'potentially unstable' regions (i.e. heavy fluid lying within light fluid) develops at lower values of Ro for anticyclones than for cyclones. It is these regions, where $\partial \hat{\Gamma}^2/\partial r < 0$, which ultimately drives the centrifugal bursting of a vortex. This is evident from a comparison of Figures 3 and 4: anticyclonic vortices very quickly develop a substantial region of negative $\hat{\Gamma}$, which then feeds the radial bursting of the vortex. Cyclonic initial conditions, on the other hand, require significantly higher values of Ro before small islands of closed $\hat{\Gamma}$-lines appear. Moreover, this phenomenon is not peculiar to the particular initial condition chosen here. It is readily confirmed that almost any simple localized region of vorticity exhibits the same asymmetry between cyclones and anticyclones. The reason is as follows: $\partial \hat{\Gamma}^2/\partial r = 2\hat{\Gamma} r(2\Omega + \omega_z)$, and regions of negative $\partial \hat{\Gamma}^2/\partial r$ first appear when $(2\Omega + \omega_z) = 0$. For an anticyclone, this occurs near the axis of symmetry where ω_z is negative and $|\omega_z|$ is relatively intense [Figure 14(b)]. For cyclones, on the other hand, this occurs at the outer edge of the vortex where $|\omega_z|$ is less intense as the vortex lines are more spread out [Figure 14(a)]. Thus $(2\Omega + \omega_z) = 0$ occurs at significantly

lower values of Ro for anticyclones. Note that this argument holds for any axisymmetric vortex blob in which the angular velocity, u_θ/r, monotonically falls with r. In all such cases we expect to see an asymmetry between cyclones and anticyclones, with anticyclones exhibiting a lower transitional value of Ro.

This is illustrated in Figure 15, where the $\hat\Gamma$-lines for cyclonic and anticyclonic vortices are shown corresponding to the different initial condition

$$\mathbf{u} = \Lambda r \exp\left[-(r^2 + z^2)/\delta^2\right]\hat{\mathbf{e}}_\theta. \tag{24}$$

As for (19), regions of negative $\partial\hat\Gamma^2/\partial r$ develop rapidly for anticyclonic initial conditions, but less rapidly for cyclones. In this case, $\partial\hat\Gamma^2/\partial r$ first becomes negative at $Ro = 0.214$ for anticyclones, but at $Ro = 1.58$ for cyclones. The ratio of the two values of Ro is 7.39. Thus we expect a substantial difference in the value of Ro at which the transition from columnar vortex formation to radial bursting occurs. It is readily confirmed that a similar picture emerges if, instead of a Gaussian fall-off in r, we choose, say, $u_\theta/r = \mathrm{sech}^2(r/\delta)$ on the symmetry plane $z = 0$. The transitional values of Ro are different, but the qualitative picture remains unchanged.

Let us now return to the sort of experiment discussed in Refs. 2 and 3 where eddies (blobs of vorticity) are created by dragging a grid through a tank of water at $Ro > 1$. With time the Rossby number falls (kinetic energy decays) and when the Rossby number falls to ~ 1, it is observed that many of the eddies start to elongate along the rotation axis, forming columnar vortices. Measurements of their rate of growth confirm that the mechanism of elongation is essentially quasi-linear inertial wave propagation, and it is usually observed that the bulk of the resulting columnar vortices are cyclonic. These observations are entirely consistent with the picture suggested above; as Ro falls it is the cyclonic eddies which first become prone to

22

columnar vortex formation. Anticyclonic vortices, on the other hand, require a substantially lower value of Ro in order to produce columnar structures. While this does not prove that the mechanism described here is *the* mechanism responsible for the dominance of cyclones, it is certainly consistent with the experimental observations. Moreover, our explanation is more in line with the experimental data than that of Gence and Frick,[8] which relies on a very special initial condition.

7 Conclusion

We have looked at the process of columnar vortex formation in a rotating fluid and shown that, when $Ro \sim 1$, cyclonic eddies are more likely to form columnar structures than anticyclonic eddies. Although the numerical simulations were for a particular class of initial conditions, we have shown that the primary conclusions are likely to hold for any simple, axisymmetric vortex. The relationship between our findings and the observation that cyclones predominate in rapidly rotating turbulence is uncertain, since our model problem is somewhat idealized. Nevertheless, our findings are consistent with the experiments on homogeneous turbulence.

8   References

[1] E.J. Hopfinger, F.K. Browand and Y. Gagne, Turbulence and waves in a rotating tank, J. Fluid Mech., **125**, 505 (1982).

[2] P.A. Davidson, P.J. Staplehurst and S.B. Dalziel, On the evolution of eddies in a rapidly rotating system, J. Fluid Mech., **557**, 135 (2006).

[3] P.J. Staplehurst, P.A. Davidson and S.B. Dalziel, Structure formation in homogeneous, freely-decaying, rotating turbulence, J. Fluid Mech., **598**, 81 (2008).

[4] P. Bartello, O. Métais and M. Lesieur, Coherent structures in rotating three-dimensional turbulence, J. Fluid Mech., **273**, 1 (1994).

[5] L. J. A. van Bokhoven, C. Cambon, L. Liechtenstein, F. S. Godeferd and H. J. H. Clercx, Refined vorticity statistics of decaying rotating three-dimensional turbulence, J. Turbulence, **9**, N6 (2008).

[6] L. Bourouiba and P. Bartello, The intermediate Rossby number range and two-dimensional-three-dimensional transfers in rotating decaying homogeneous turbulence, J. Fluid Mech., **587**, 139 (2007).

[7] C. Morize, F. Moisy and M. Rabaud, Decaying grid-generated turbulence in a rotating tank, Phys. Fluids, **17**, 045105 (2005).

[8] J.- N. Gence and C. Frick, Naissance des correlations triples de vorticité dans une turbulence homogéne soumise à une rotation, C.R. Acad. Sci. Paris II, **329**, 351 (2001).

[9] P.A. Davidson, B. Sreenivasan and A.J. Aspden, Evolution of localized blobs of swirling or buoyant fluid with and without an ambient magnetic field, Phys. Rev. E, **75**, 026304

(2007).

[10] L.M. Polvani, J.C. McWilliams, M. Spall and R. Ford, The coherent structures of shallow water turbulence: deformation radius effects, cyclone/anticyclone asymmetry and gravity wave generation, Chaos, **4**, 177 (1994)

[11] G.J. Hakim, C. Snyder, and D. J. Muraki, A new surface model for cyclone-anticyclone asymmetry, J. Atmos. Sci., **59**, 2405 (2002).

[12] G. Perret, A. Stegner, M. Farge, and T. Pichon, Cyclone-anticyclone asymmetry of large-scale wakes in the laboratory, Phys. Fluids, **18**, 036603 (2006).

[13] L.P. Graves, J.C. McWilliams, and M.T. Montgomery, Vortex evolution due to straining: a mechanism for dominance of strong, interior anticyclones, Geophys. Astrophys. Fluid Dynam., **100**, 151 (2006).

[14] H. Goldstein, *Classical Mechanics*, 2nd Edition, p 351 (Addison-Wesley, Reading, Massachusetts, 1980).

[15] P.A. Davidson, Global stability of two-dimensional and axisymmetric Euler flows, J. Fluid Mech., **276**, 273 (1994).

[16] J. Majdalani and S.W. Rienstra, On the bidirectional vortex and other similarity solutions in spherical coordinates, J. Appl. Math. Phys. (ZAMP), **58**, 289 (2007).

$\delta \Omega t$

$\delta \Omega t$

$l_z \sim \delta \Omega t$
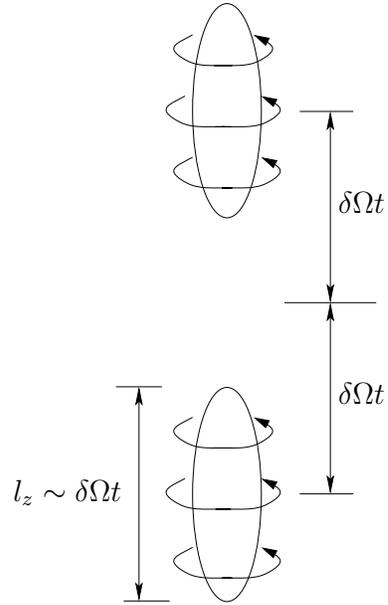
Figure 1: An initial blob of vorticity converts itself into a pair of columnar vortices via inertial wave propagation ($Ro << 1$).
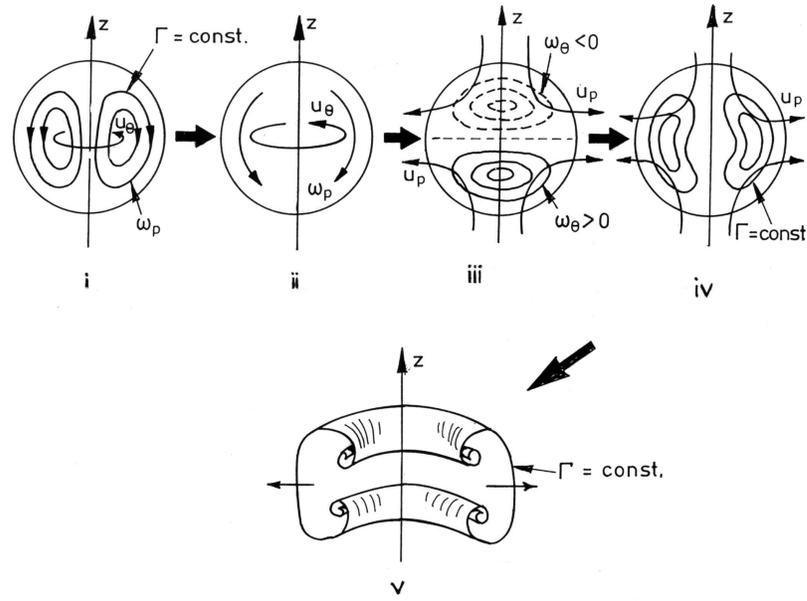
Figure 2: The centrifugal bursting of a swirling vortex ($Ro \gg 1$). (i) the initial condition; (ii) the associated poloidal vorticity; (iii) azimuthal vorticity swept out from the poloidal vorticity by differential rotation; (iv) the poloidal velocity associated with the azimuthal vorticity sweeps out the angular momentum, Γ; and (v) the eventual state.
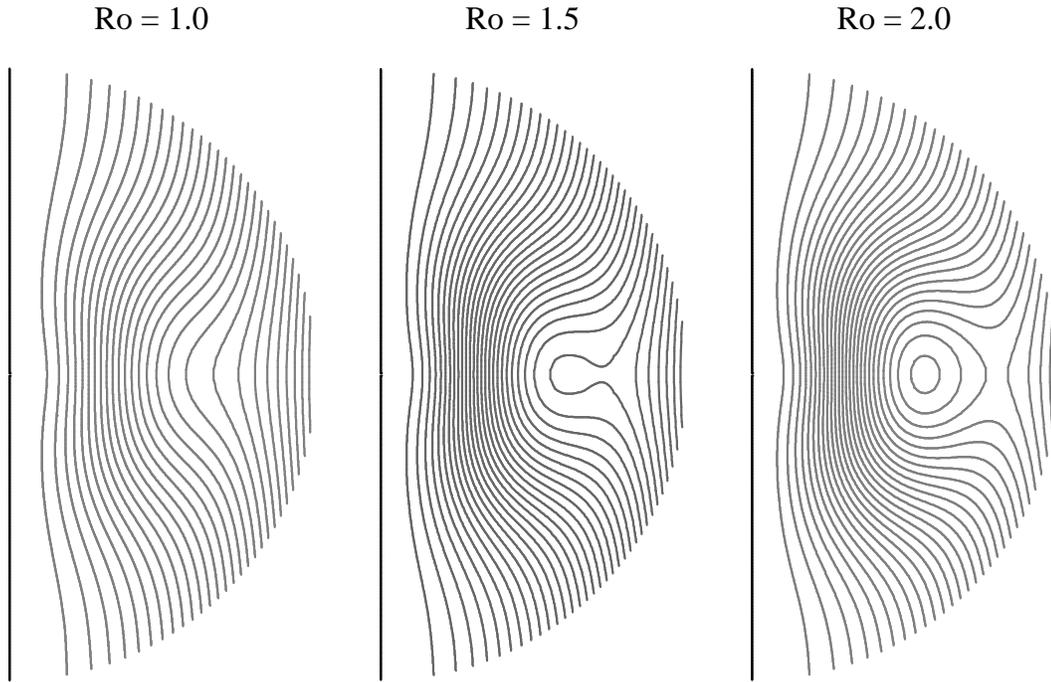
Figure 3: Lines of absolute angular momentum, $\hat{\Gamma}$, at $t = 0$ for cyclonic initial conditions. The contours are shown in the domain $R/4$.

Ro = 0.33   Ro = 0.39   Ro = 0.43   Ro = 0.45   Ro = 0.50

Ro = 0.60   Ro = 0.80   Ro = 1.0   Ro = 1.2
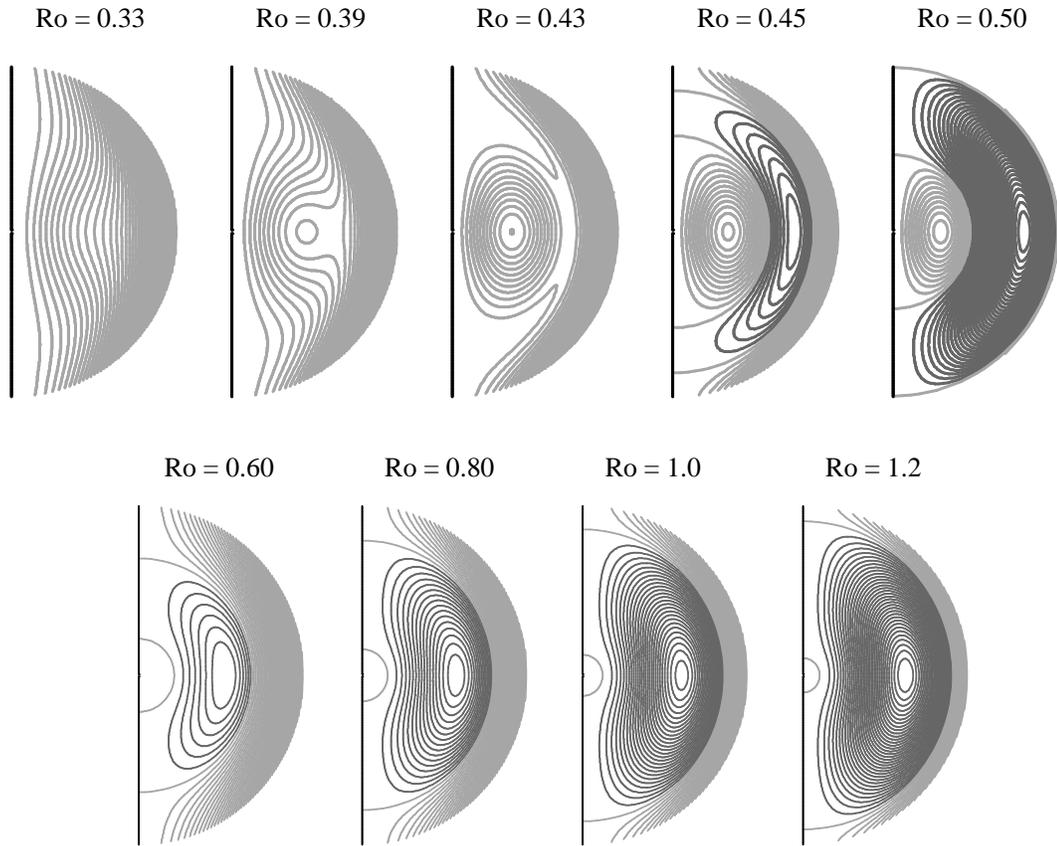
Figure 4: Lines of absolute angular momentum, $\hat{\Gamma}$, at $t = 0$ for anticyclonic initial conditions. Contours for the cases $Ro = 0.33 - 0.50$ (top row) are restricted to the domain $R/10$ and cases $Ro = 0.60 - 1.2$ (bottom row) are shown in the domain $R/6$. Light contours show positive values and dark contours show negative values.
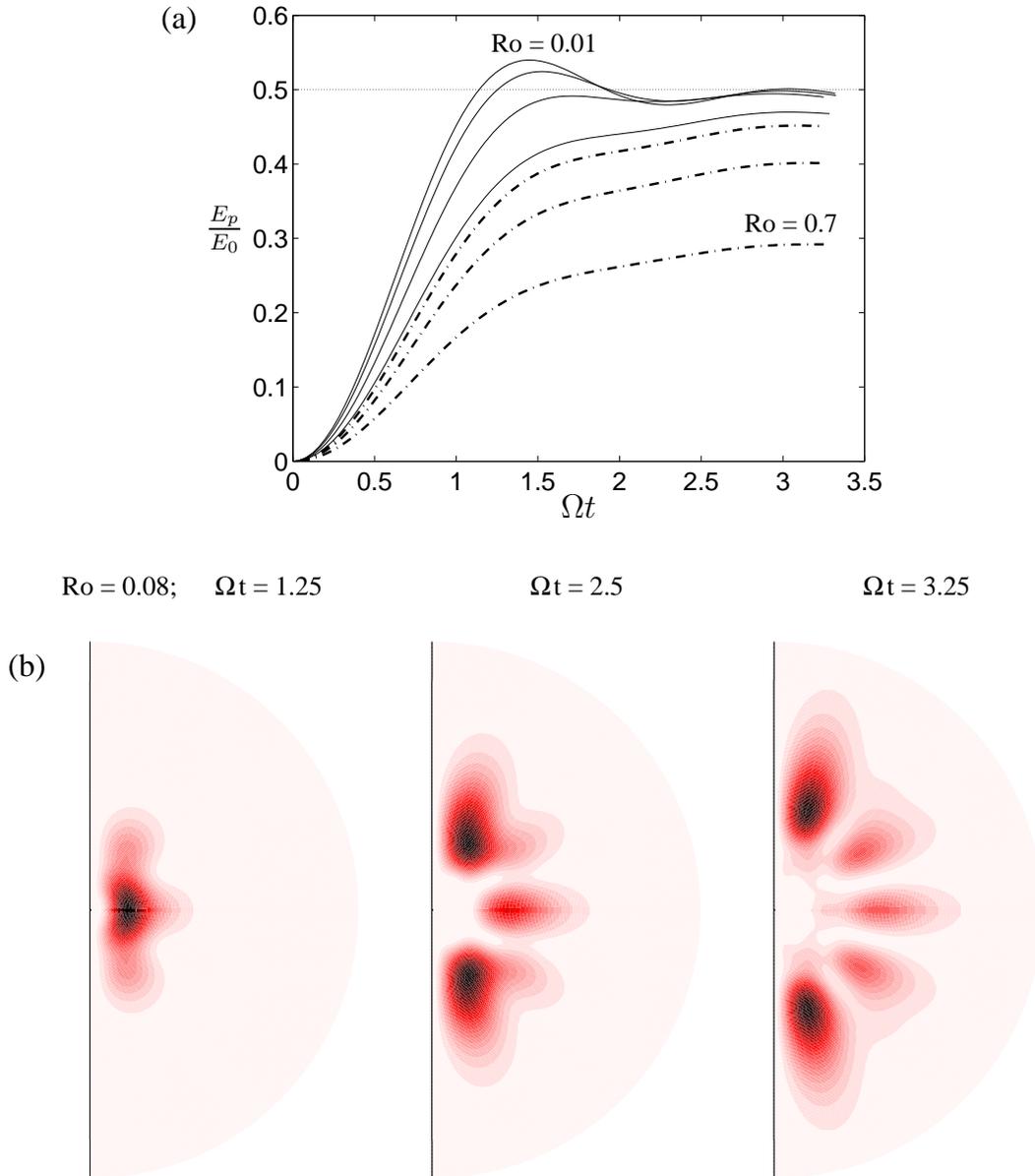
Figure 5: Evolution of an anticyclone. (a) Normalized poloidal kinetic energy, E_p/E_0, versus Ωt for $Ro = 0.01, 0.08, 0.2$ and 0.35 (solid lines from top to bottom) and for $Ro = 0.4, 0.5$ and 0.7 (dashed-dotted lines from top to bottom). (b) Shaded contours of azimuthal kinetic energy, $\frac{1}{2}u_\theta^2$, for $Ro = 0.08$ at $\Omega t = 1.25, 2.5$ and 3.25, shown for the restricted domain $2R/3$.

30
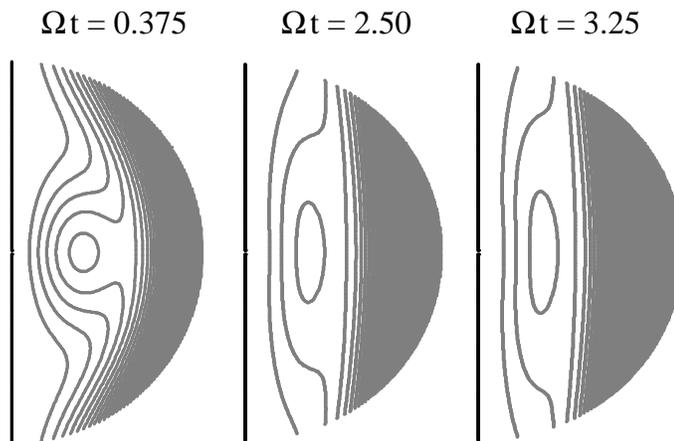
Figure 6: Flow corresponding to $Ro = 0.4$ (anticyclonic initial condition). Contours of absolute angular momentum, $\hat{\Gamma}$ at different times, shown for the restricted domain $R/10$.

$\Omega t = 0.6$ $\Omega t = 1.2$ $\Omega t = 1.8$ $\Omega t = 2.4$

(a)

$\Omega t = 3.3$

(b)   (c)

PSfrag replacements
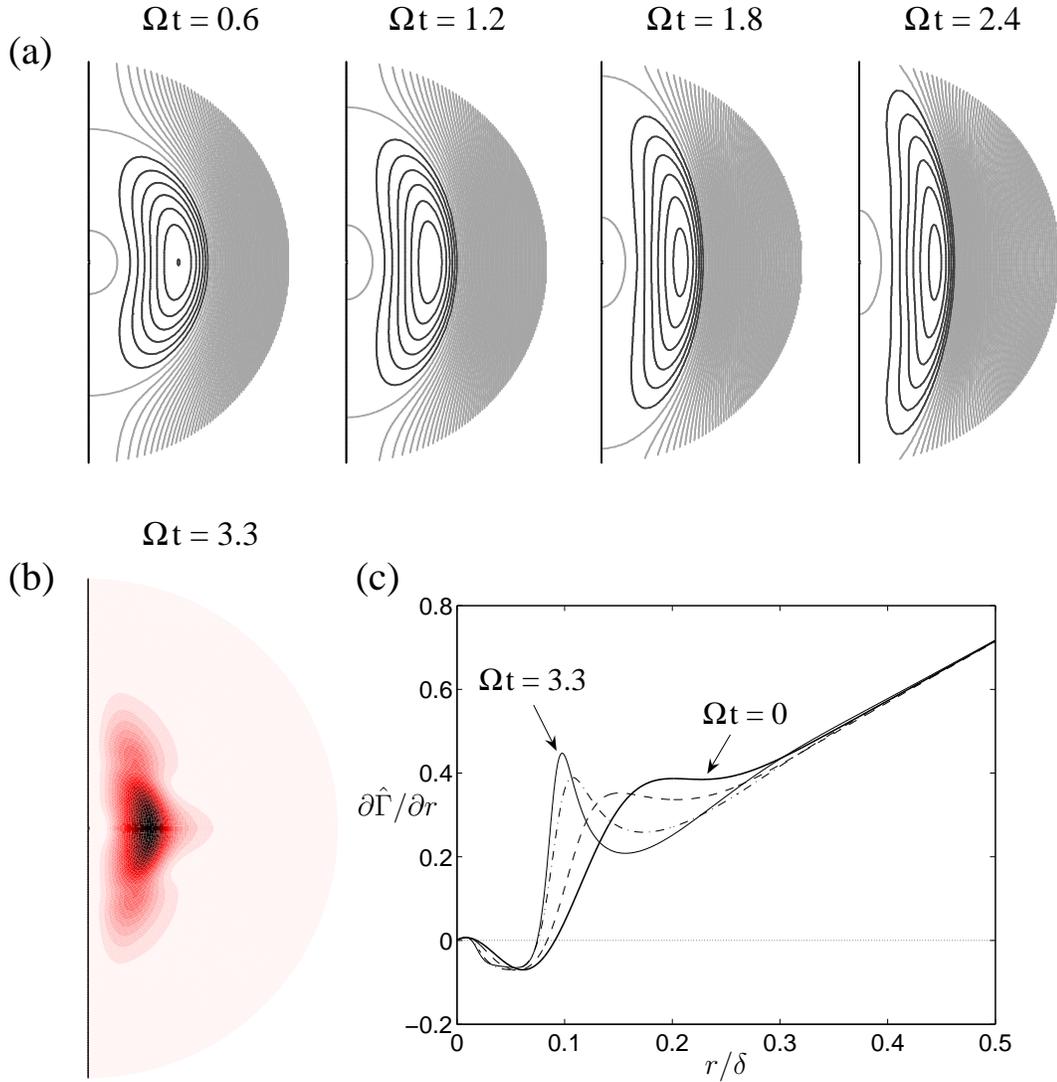
Figure 7: Flow for $Ro = 0.7$ (anticyclonic initial condition). (a) Contours of $\hat{\Gamma}$ for different times, shown for the restricted domain $R/5$. Light contours show positive values and dark contours show negative values. (b) Contours of azimuthal kinetic energy, $\frac{1}{2}u_\theta^2$, at $\Omega t = 3.0$, shown for the restricted domain $R/3$. (c) $\partial\hat{\Gamma}/\partial r$ on the symmetry plane versus r/δ for $\Omega t = 0$ (thick solid line), 1.2 (dashed line), 2.4 (dashed-dotted line) and 3.3 (thin solid line).

32

$Ro = 1.4; \; \Omega t = 0.6$ $\Omega t = 1.2$ $\Omega t = 1.8$

(a)

(b)

$\partial\hat{\Gamma}/\partial r$

r/δ

(i) Ro = 1.0   (ii) Ro = 1.4   (iii) Ro = 1.8

PSfrag replacements
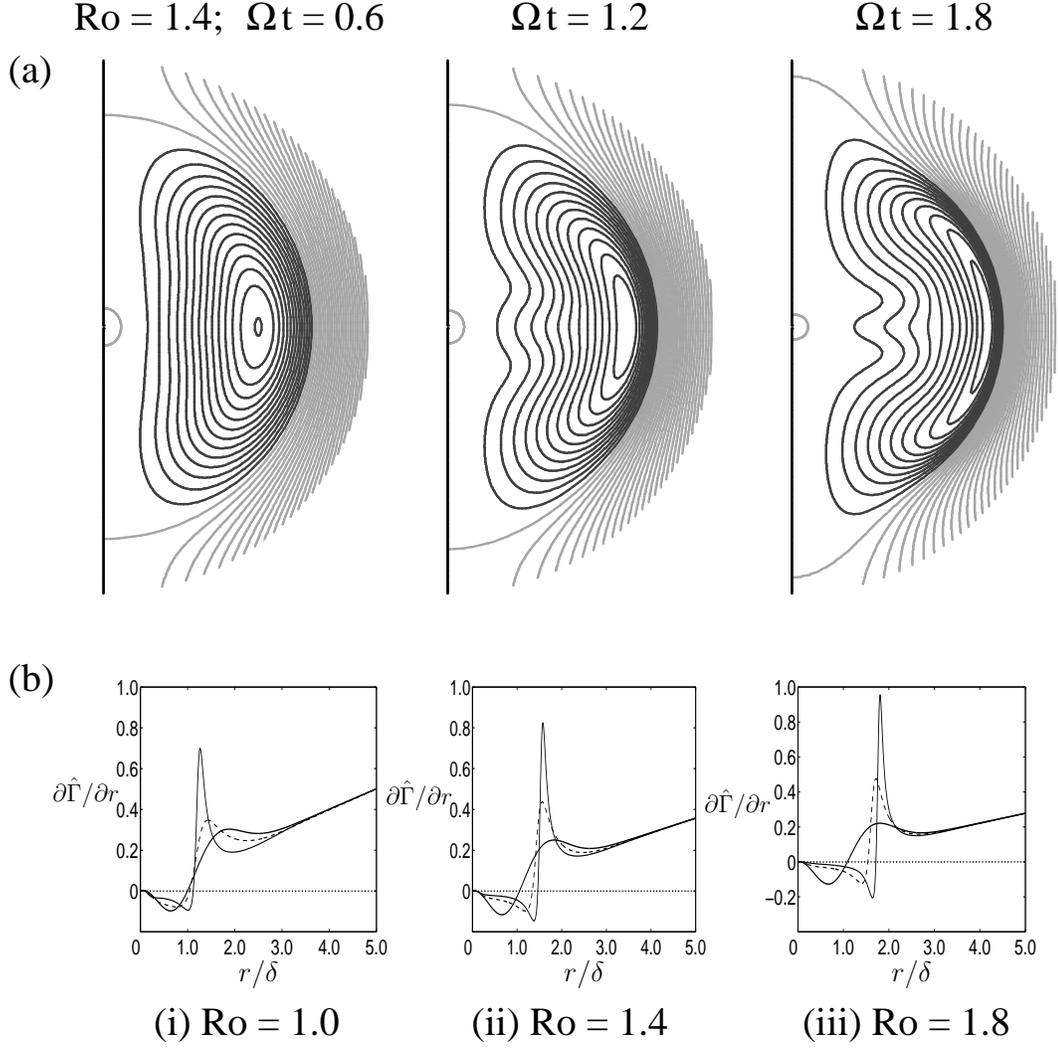
Figure 8: (a) Contours of the absolute angular momentum, $\hat{\Gamma}$, for anticyclonic initial conditions and $Ro = 1.4$, shown for different times in the restricted domain $R/5$. (b) $\partial\hat{\Gamma}/\partial r$ on the symmetry plane for anticyclonic initial conditions. (i) $Ro = 1$ and $\Omega t = 0, 1.25, 2.5$ (thick solid line, dashed line, thin solid line); (ii) $Ro = 1.4$ and $\Omega t = 0, 1.2, 1.8$ (thick solid, dashed, thin solid); (iii) $Ro = 1.8$ and $\Omega t = 0, 1.0, 1.5$ (thick solid, dashed, thin solid).

33
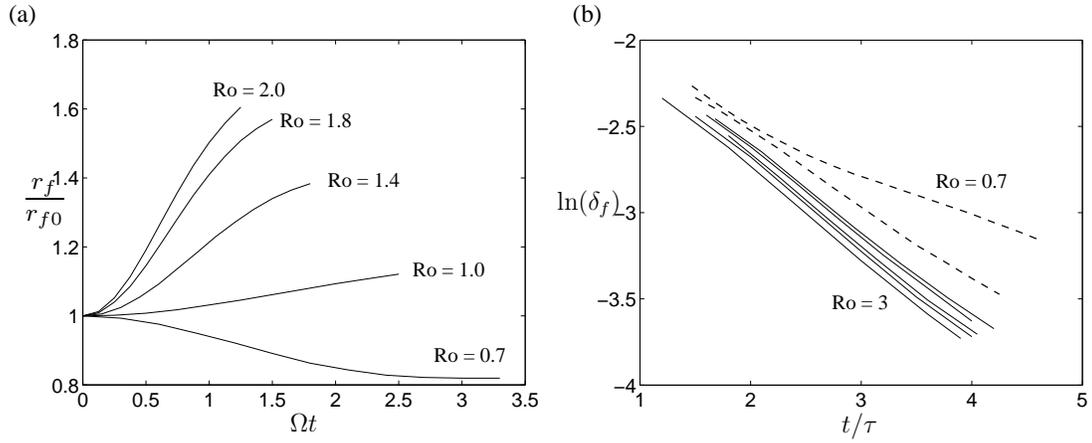
Figure 9: Front position, r_f, and front thickness, δ_f, for anticyclonic initial conditions. (a) r_f/r_{f0} versus Ωt for different Rossby numbers shown. (b) $\ln(\delta_f)$ versus t/τ. The curves from top to bottom correspond to the cases $Ro = 0.7, 1.0$ (both in dashed lines), $Ro = 1.4, 1.6, 1.8, 2.0, 3.0$ (in solid lines).

(a)

(b)

$\partial \hat{\Gamma} / \partial r$

PSfrag replacements

r/δ
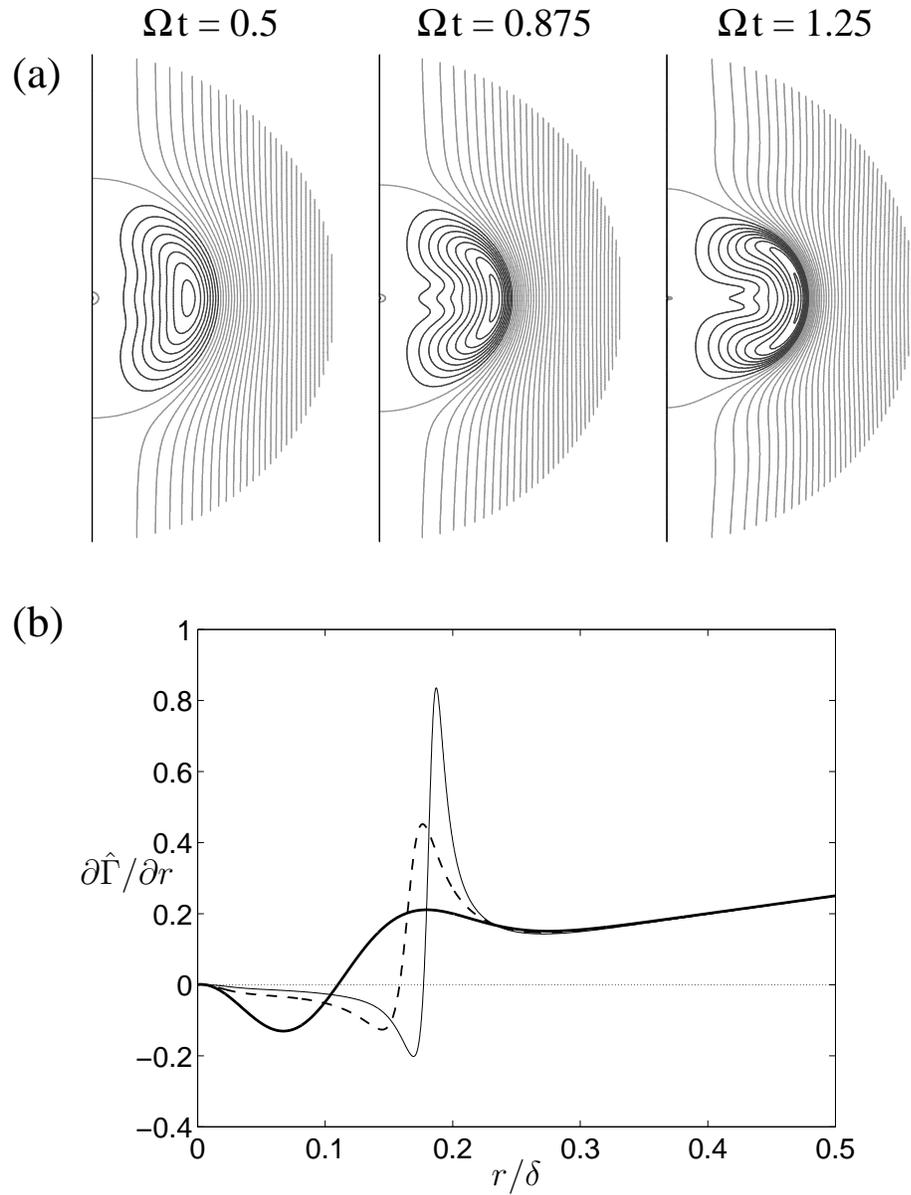
Figure 10: Flow for anticyclonic initial conditions and $Ro = 2.0$. (a) Contours of $\hat{\Gamma}$ at $\Omega t = 0.5, 0.875$ and 1.25, shown for the restricted domain $R/3$. (b) $\partial \hat{\Gamma}/\partial r$ on the symmetry plane at $\Omega t = 0.0, 0.875$ and 1.25 (thick solid line, dashed line, thin solid line).

Ro = 1.0   Ro = 2.0   Ro = 3.0   Ro = 4.0
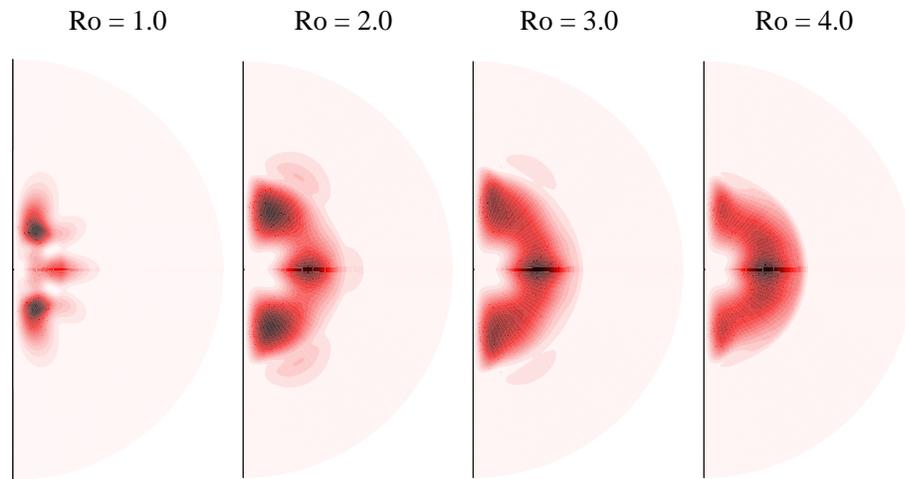
Figure 11: Azimuthal energy density for cyclonic initial conditions shown for the restricted domain $R/2$. $Ro = 1.0$, $\Omega t = 2.5$; $Ro = 2.0$, $\Omega t = 1.0$; $Ro = 3.0$, $\Omega t = 0.8$; $Ro = 4.0$, $\Omega t = 0.5$.
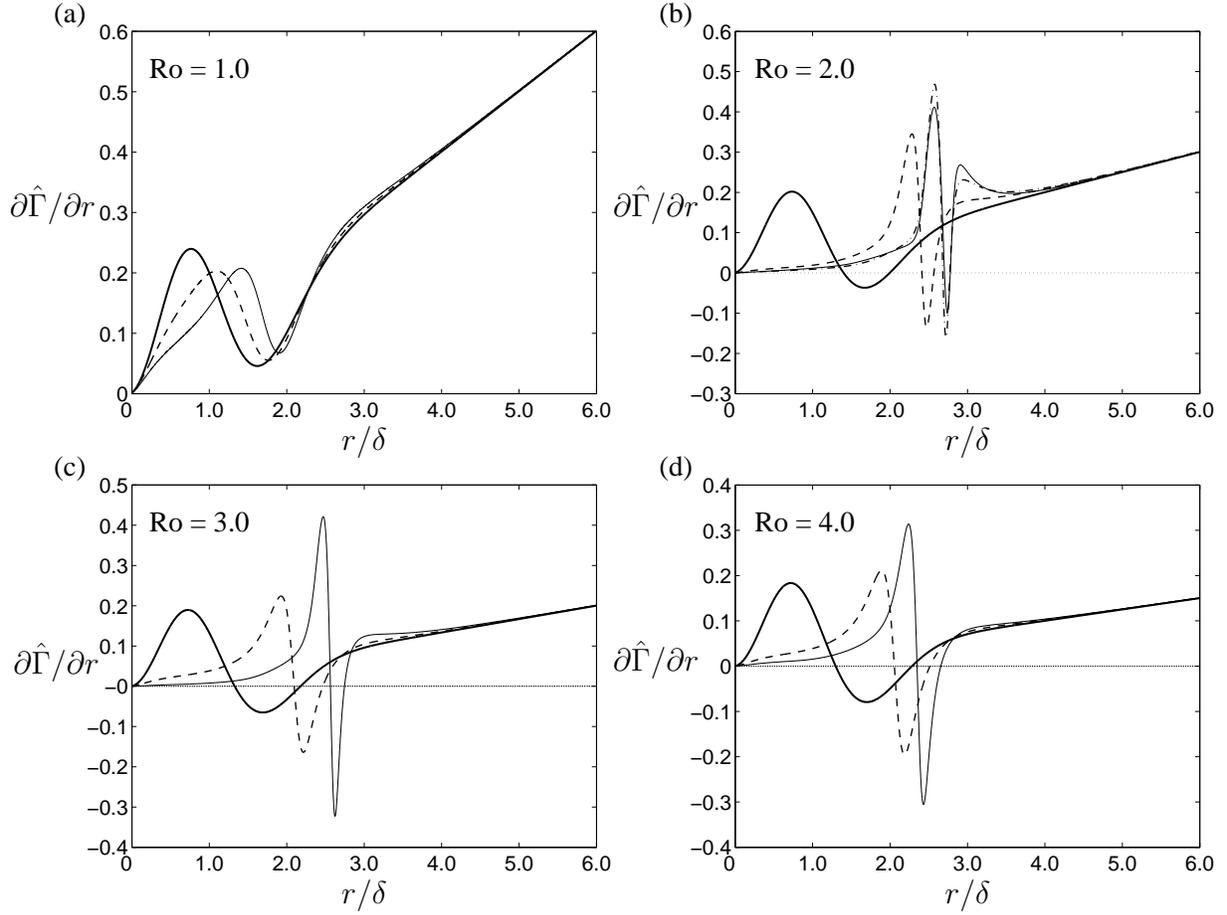
Figure 12: The evolution of $\partial\hat{\Gamma}/\partial r$ on the symmetry plane $z = 0$ for cyclonic initial conditions: (a) $Ro = 1.0$, for $\Omega t = 0$ (thick solid line), 0.5 (dashed line) and 0.75 (thin solid line); (b) $Ro = 2.0$, for $\Omega t = 0$ (thick solid line), 1.0 (dashed), 1.5 (dashed-dotted) and 2.0 (thin solid); (c) $Ro = 3.0$, for $\Omega t = 0$ (thick solid), 0.5 (dashed) and 0.8 (thin solid); (d) $Ro = 4.0$, for $\Omega t = 0$ (thick solid), 0.375 (dashed) and 0.5 (thin solid).

37
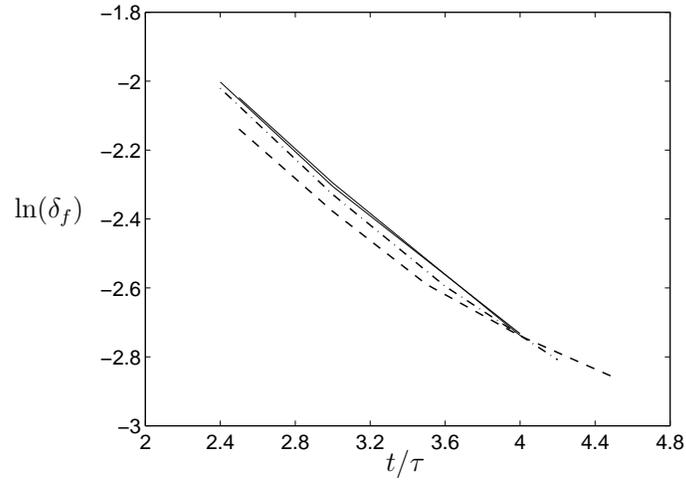
Figure 13: $\ln(\delta_f)$ versus t/τ for $Ro = 2$ (dashed), $Ro = 3$ (dashed-dotted), $Ro = 4, 5$ (solid lines), for cyclonic initial conditions.

(a) (b)
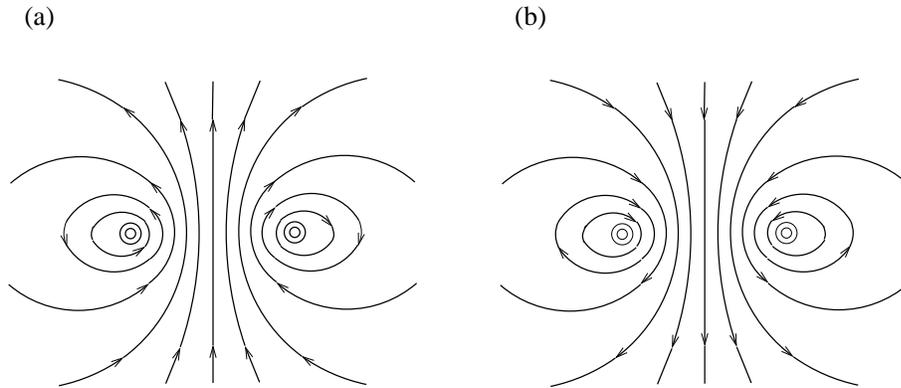
Figure 14: Poloidal vortex lines, ω_p, at $t = 0$, for (a) a cyclonic vortex; (b) an anticyclonic vortex.

38
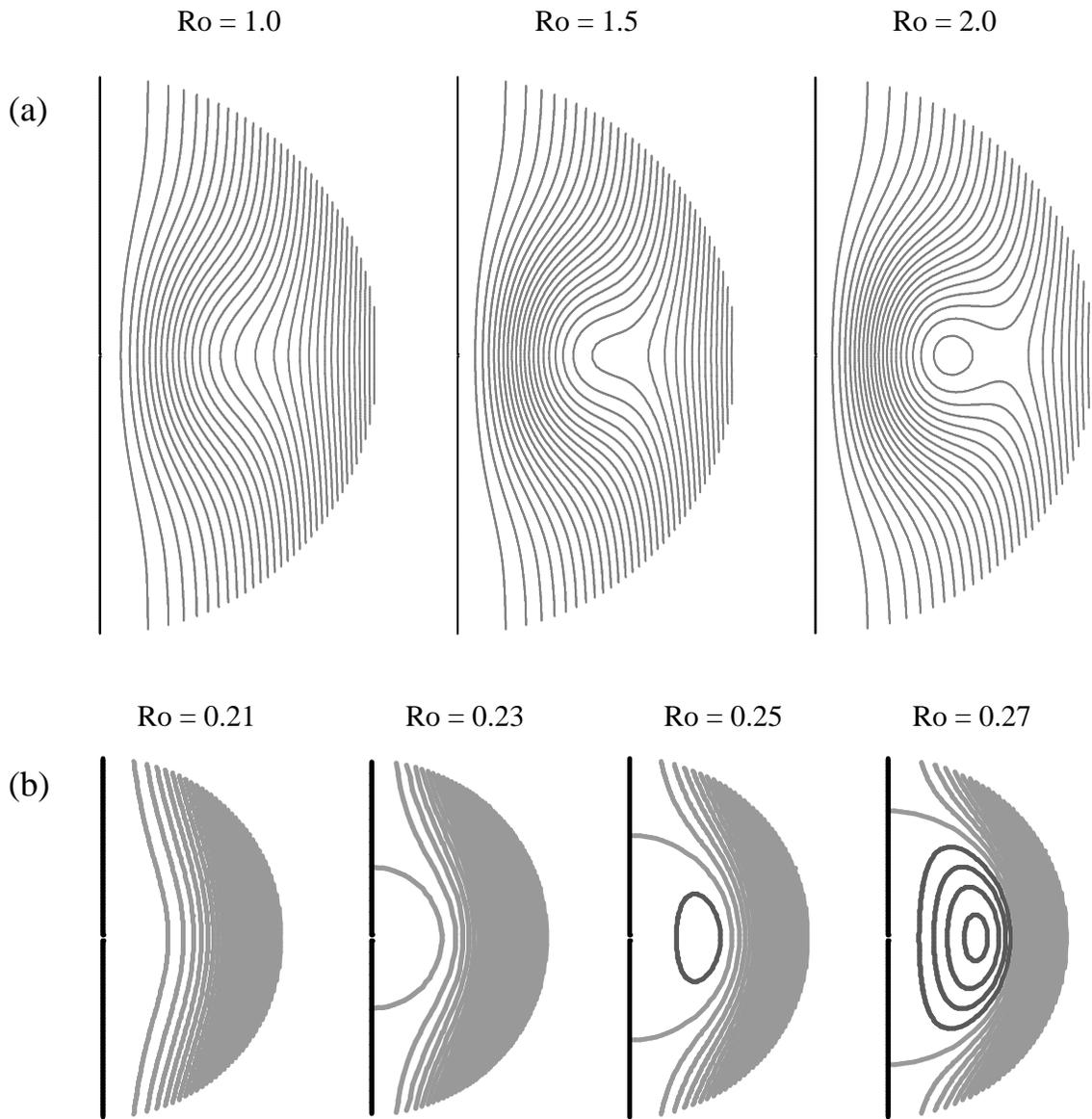
Figure 15: (a) Contours of absolute angular momentum, $\hat{\Gamma}$, at $t = 0$ for a cyclonic vortex corresponding to (24). The plots are restricted to the domain $R/4$. (b) Contours of $\hat{\Gamma}$ at $t = 0$ for an anticyclonic vortex corresponding to (24). The plots are restricted to the domain $R/15$. Light contours show positive values and dark contours show negative values.

39